Petroleum Science 22 (2025) 5228–5238

Contents lists available at ScienceDirect

Petroleum Science

journal homepage: www.keaipublishing.com/en/journals/petroleum-science

Original Paper

Molecular dynamics simulation of methane isotope fractionation in two-phase flow within inorganic pores

Pei-Qi Xu [a,c], Wei Chen [a,b,c,*]

[a] School of Rail Transportation, Soochow University, Suzhou 215131, Jiangsu, China
[b] Key Laboratory of Coalbed Methane Resources and Reservoir Formation Process of the Ministry of Education, China University of Mining and Technology, Xuzhou, 221008, Jiangsu, China
[c] Jiangsu Provincial Smart Urban Rail Engineering Research Center, Suzhou, 215131, Jiangsu, China

A R T I C L E I N F O

Article history:
Received 14 March 2025
Received in revised form
6 May 2025
Accepted 25 July 2025
Available online 31 July 2025

Edited by Min Li

Keywords:
Shale gas
Isotopic fractionation
Inorganic pores
Water saturation
Molecular dynamics simulations

A B S T R A C T

Carbon isotope fractionation served as a key geochemical indicator for understanding shale gas storage and migration. However, the detailed mechanism of the fractionation behaviors of methane isotopes ($^{12}CH_4/^{13}CH_4$) was still limited, especially under two-phase flow. This study employed molecular dynamics (MD) simulations to investigate water-mediated nonlinear isotope transport in 3 nm hydrophilic silica nanopores, highlighting gas-liquid-solid interfacial effects on fractionation mechanisms. Simulations of different water saturation (0%–44.66%) showed a critical hydration threshold of 30.44% at a pressure gradient of 20 MPa. Below this threshold, continuous water film formed on pore walls, which transformed the gas transport from surface diffusion to viscous flow through gas-liquid interactions, while hydrogen bonds in the water film weakened gas-solid slip effects. However, when water saturation exceeded 30.44%, the formation of water bridges blocked the mobility of isotopic gases. The water film reduced the depth of solid-gas potential wells, leading to diminished adsorption capacity for isotopic gases, and lowered the surface roughness of pore walls (as characterized by potential energy surface, PES). Additionally, the water film enhanced the Knudsen diffusion effect of isotope gases due to the decrease in effective pore size. As a result, the formation of water film intensified methane isotopic fractionation, which was manifested as a decrease in the $^{13}CH_4/^{12}CH_4$ diffusion coefficient ratio (D^*/D) from 0.975 to 0.942 and an increase in isotopic enthalpy differences ($\Delta h_{^{12}C\_^{13}C}$) from 0.105 to 1.139 J/m^3. Furthermore, in the gas-liquid-solid interfacial system, an elevated pressure differential modified the relative motion velocities among the methane-water-pore surface, resulting a non-monotonic isotopic fractionation trend (initial increase followed by decrease). These findings provided molecular-level insights into the complex isotopic fractionation in shale gas systems.

1. Introduction

As essential clean energy resources, shale gas and coalbed methane (CBM) have gained growing significance in global energy supplies (Wan et al., 2023; Chen et al., 2024). The efficient exploitation of shale gas poses challenges owing to its limited porosity and permeability (Sun et al., 2021; Feng et al., 2023; Xiao et al., 2023). Due to the multiple transport mechanisms of methane (e.g., Fick diffusion, Knudsen diffusion, slip flow, and Darcy flow) in nanopores and its complex flow characteristics, predicting production capacity is challenging (Chen and Horne, 2006; Yu et al., 2020a). Therefore, isotope tracer technology is needed to study and understand these processes more effectively (Sun et al., 2018). Recently, the isotopic composition of methane has been used to estimate the gas saturation of shale reservoirs and reveal the characteristics of gas production stages for the tight shale gas formations, the genesis, migration mode and maturity of shale gas (Qu et al., 2016; Yu et al., 2020c).

The transition from continuous flow to non-equilibrium transport states (e.g., Knudsen diffusion) in nanoscale pores induces mass-dependent kinetic fractionation in methane isotopes

* Corresponding author.
E-mail address: timtamu@suda.edu.cn (W. Chen).
Peer review under the responsibility of China University of Petroleum (Beijing).

https://doi.org/10.1016/j.petsci.2025.07.019

(Mo et al., 2022; Wang et al., 2022). Heavier $^{13}CH_4$ molecules exhibit enhanced energy dissipation compared to $^{12}CH_4$ molecules due to isotopic mass-modulated collision cross-sections, adsorption-desorption hysteresis, and translational-rotational decoupling (Chen et al., 2020; Xia and Tang, 2012). This velocity differential drives isotopic separation and challenges the classical fluid dynamics models of gas transport in unconventional reservoirs (Wu et al., 2015; Veltzke and Thöming, 2012). In addition, the activation energy required for the diffusion of $^{13}CH_4$ molecules is slightly higher than that of $^{12}CH_4$ molecules, which further enhances the isotope fractionation process (Zhang et al., 2025). Methane isotope fractionation is governed by pore-scale physicochemical controls, including organic/inorganic pore architecture, surface topographic heterogeneity, and interfacial wettability dynamics (Zhang et al., 2020b; Gong et al., 2020). The amplitude of carbon isotope fractionation scales positively with total organic carbon (TOC) saturation and inversely with clay mineral abundance (Wei et al., 2021; Liu et al., 2023). In addition, molecular dynamics simulations revealed that the degree of isotope fractionation in organic pores (OP) was more significant than that in inorganic pores (IP) (Wang et al., 2021a). This is because the high-coverage adsorption in OP enhances the Knudsen diffusion effect by reducing the effective pore size, thereby increasing the level of carbon isotope fractionation (Xia and Tang, 2012; Chen et al., 2023). Moreover, compared with inorganic pores, the surface of organic pores is smoother, and their frequent specular reflection enhances the difference in diffusion ability of $^{12}CH_4$ and $^{13}CH_4$ isotopes (Wang et al., 2021a).

Organic and inorganic pores in shale exhibit distinct wettability characteristics, with organic pores typically being hydrophobic and inorganic pores hydrophilic (Zhang et al., 2020a; Arif et al., 2021). This difference in wettability, combined with the ubiquity of moisture in shale nanopores, regulates the transport and storage mechanisms of fluids (Wang et al., 2017a). In hydrophobic organic pores, water molecules are concentrated to form water clusters, whereas in hydrophilic inorganic pores, water forms layered films on the pore surface (Xu et al., 2020; Zhang et al., 2019; Xiang et al., 2014). The water molecules within the shale matrix not only affect the adsorption behavior of methane isotopes, but also significantly influence their transport capacity (Babaei et al., 2023; Mo et al., 2020). Specifically, hydrophilic inorganic pores preferentially adsorb water, reducing methane isotope adsorption affinity (Wang et al., 2017b; Liu et al., 2018). Concurrently, the water film diminishes effective pore radius, imposing nanoconfinement effects that restrict gas flow and suppress isotopic diffusion (Bui et al., 2017). The presence of water film changes the roughness of the surface of the inorganic pore wall (Yang et al., 2024), influencing methane isotopes' mobility, slip behavior, and isotopic fractionation dynamics (Zhan et al., 2020; Nan et al., 2020). However, this critical mechanism remains underexplored in current research.

Methane isotope molecules and water molecules exhibit a complex two-phase transport process in the shale nanopores (Yu et al., 2020c; Mo et al., 2020). The nonlinear adsorption/desorption and diffusion behaviors of water and gas molecules result not only in molecular fractionation but also in isotope fractionation (Liu et al., 2020). In the presence of water, the interaction dynamics shift from gas-solid interactions to more complex gas-liquid-solid interactions (Qin and Suckale, 2017). In the gas-solid interaction stage, methane isotope molecules are mainly bound to the pore wall surface through weak interaction forces such as Van der Waals forces and electrostatic forces (Zhang et al., 2020b). However, the presence of water molecules leads to strong interaction forces such as hydrogen bonds between methane isotope molecules and the solid surface of the pore wall (Merzel and Avbelj, 2020; He et al., 2014). This action leads to an anisotropic change in the angular distribution function of methane molecules after collision, which deviates from the classical Knudsen diffusion model (Aranovich and Donohue, 2009). Thus, different intermolecular collisions between methane isotopes, water molecules and pore walls, as well as different collision frequencies, lead to different momentum losses during molecular transport, thereby causing changes in isotope fractionation (Richter et al., 2006).

Although there are many relevant studies on the flow dynamics of methane and water in shale matrices, significant gaps remain in the research on the isotopic fractionation of inorganic pore two-phase flow in shale reservoirs. Under these conditions, the particular alterations in methane isotope fractionation remain inadequately investigated.

In this research, grand canonical Monte Carlo (GCMC) and molecular dynamics simulations (MD) were employed to explore the carbon isotope fractionation of methane ($^{12}CH_4$ and $^{13}CH_4$) within inorganic nanopore under two-phase flow conditions. Firstly, the impact of water saturation on the existence state of isotope gas molecules within inorganic pore channels was studied. Secondly, the variations in specific enthalpy and diffusion behavior of isotope gases under different water molecular saturations were compared. Finally, the effect of the presence of water on the diffusion process of isotopes and the degree of fractionation in hydrophilic nanopores were analyzed via water-solid-gas interactions.

2. Simulation details

The shale matrix consists of inorganic and organic materials, with silica being a key mineral found in numerous shale formations (Gong et al., 2020; Hantal et al., 2014). Therefore, a silica channel with dimensions of x = 4.4 nm, y = 13.5 nm, and z = 6.1 nm, featuring the pore diameter of 3 nm, has been constructed for simulating isotope fractionation in a gas-water two-phase flow system as illustrated in Fig. 1. At the initial stage of the simulation, methane and water molecules were randomly distributed within the nanochannels. As the system reached equilibrium state, a distinct phase separation between methane and water became evident (Fig. 2).

2.1. Molecular models

Van der Waals interactions are pivotal in shaping the dynamic interplay between pore wall atoms and isotopic gas molecules, namely $^{12}CH_4$ and $^{13}CH_4$. The relationship between these gas molecules and the wall atoms is characterized by the 12-6 Lennard-Jones (12-6 LJ) potential (Martin and Siepmann, 1998).

$$u_{\mathrm{LJ}}\left(r_{ij}\right) = 4\varepsilon_{ij}\left[\left(\frac{\sigma_{ij}}{r_{ij}}\right)^{12} - \left(\frac{\sigma_{ij}}{r_{ij}}\right)^{6}\right] \tag{1}$$

where, r_{ij} is the distance separating the molecules at the sites i and j, ε_{ij} and σ_{ij} represent the potential well depth and its zero-crossing distance, respectively. The values of ε_{ij} and σ_{ij} for various atom types are determined using the standard Lorentz-Berthelot mixing rules

$$\varepsilon_{ij} = \sqrt{\varepsilon_i \cdot \varepsilon_j}\ \sigma_{ij} = \left(\sigma_i + \sigma_j\right) \Big/ 2 \tag{2}$$

The parameters of silicon dioxide, water molecules, and methane molecules were detailed in Table 1.

Isotopic methane molecules were regarded as a single atom model because they possess relatively weak octupole moments.

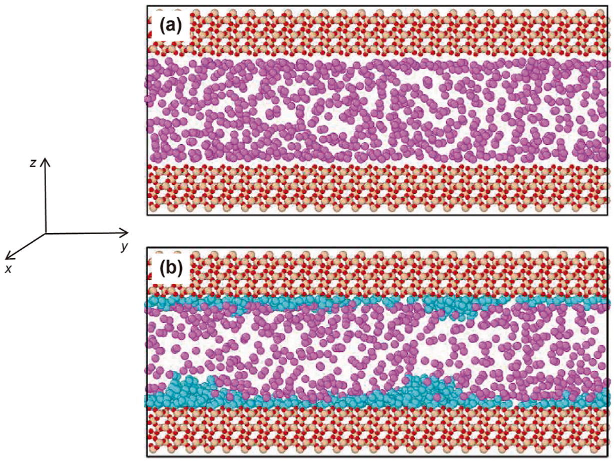

Fig. 1. Model of methane and water transport in silica nanopores: **(a)** no water in the model channel; **(b)** coexistence of methane and water in the model channel. The green spots represent water molecules, and the purple spheres are methane molecules.

For water molecules, the SPC/E model was adopted, considering water as a rigid molecule. The long-range electrostatic forces were calculated using the particle-particle-particle-mesh (PPPM) method with a precision of 10^{-4} (Darden et al., 1993). The SHAKE algorithm was employed to constrain the O–H bond and the H–O–H angle, which maintained the geometry of the water molecule during the simulation.

The cutoff distance was established at 1.35 nm, with shift correction implemented to the LJ interactions. All simulations were performed using the Large-Scale Atomic-Molecular Massively Parallel Simulator (LAMMPS) software.

2.2. NEMD simulations

In the research, the GCMC simulation method was employed to investigate the generation process of methane molecules in inorganic nanopores with varying quantities of water molecules. In addition, the non-ideal gas effect in enclosed geometry needs to be considered, and the fugacity coefficient in the GCMC simulation was set by adopting the Peng-Robinson equation of state (Wang et al., 2019; Thomas and McGaughey, 2009). In the GCMC simulation, the number of water molecules in the two-phase flow was set between 0 and 800, and the temperature was regulated by the Nose-Hoover thermostat and set at 350 K (Wang et al., 2021b). Each GCMC simulation lasted for 1×10^5 steps with a duration of 1 fs per step. Equilibrium molecular dynamics (EMD) simulations were conducted to characterize the spatial distribution of methane isotopes and water molecules in inorganic nanopores. Analysis was performed on the final 2 ns of equilibrated trajectories to ensure statistical reliability. The composition of the simulation system and the corresponding water saturation were summarized in Table 2.

Table 1
LJ force field parameters and particle charges for MD simulations (Chen et al., 2017; Zhang et al., 2021; Randall and Andrey, 2004).

Particle type	Mass, g/mol	ε, kcal/mol	σ, Å	q, e
O (H_2O)	15.999	0.155	3.166	−0.8476
H (H_2O)	1.008	0	0	0.4238
$^{12}CH_4$	16	0.294	3.750	0
$^{13}CH_4$	17	0.294	3.750	0
S_i	28.086	1.84×10^{-6}	3.302	2.1000
O (S_iO_2)	15.999	0.155	3.166	−1.0500

After obtaining the equilibrium configuration, the transport properties of isotopes ($^{12}CH_4$ and $^{13}CH_4$) in the two-phase flow of inorganic nanopores were investigated using non-equilibrium molecular dynamics (NEMD) simulations. To stimulate flow through the nanopores, an equal external force was exerted on each molecule in the flow direction (y-direction). The force can be expressed as follows (Todd et al., 1995):

$$f = \frac{\Delta P \times A}{N} \tag{3}$$

where N represents the number of fluid molecules within the system (including methane isotope molecules and water molecules) and A is the cross-sectional area of the inorganic pores.

The NEMD simulation was conducted under the canonical ensemble (NVT). To eliminate the effect of transfer velocity, in the NEMD simulation, the Nose-Hoover thermostat was linked to the fluid degrees of freedom perpendicular to the direction of flow. The total duration of the simulation was 20 ns, and data collection was conducted during the final 15 ns after the system reached a steady state.

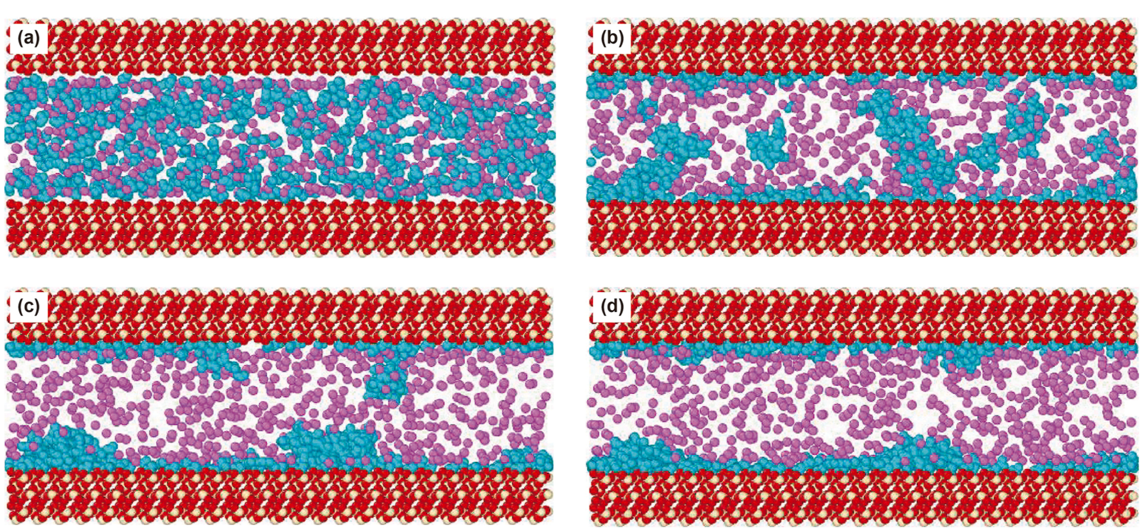

Fig. 2. A snapshot of water molecules and methane molecules during the simulation.

Table 2
The composition of the simulation system (water saturation is calculated by equation $S_w = \frac{V_{H_2O}}{V_{pore}} \times 100\%$).

Water molecules	Methane molecules	Water saturation, %
0	915	0
200	871	7.61
400	802	15.23
600	776	30.44
800	704	44.66

2.3. Definitions

2.3.1. Slip length

The slip is caused by the friction force and shear stress of the liquid on the interface, and the slip length is the extrapolated distance relative to the interface where the fluid velocity vanishes (Nan et al., 2020). The slip lengths of isotopologues (L_s and L_{s^*}, where the parameters with asterisks refer to $^{13}CH_4$) are as follows

$$\begin{cases} L_s = \dfrac{R}{3}\left(\dfrac{8\mu Q}{\left(\dfrac{\partial p}{\partial z}\right)\pi R^4} - 1\right) \\ L_{s^*} = \dfrac{R}{3}\left(\dfrac{8\mu^* Q^*}{\left(\dfrac{\partial p}{\partial z}\right)\pi R^4} - 1\right) \end{cases} \tag{4}$$

where R represents the pore radius, μ denotes the viscosity, $\frac{\partial p}{\partial z}$ indicates the pressure gradient, Q denotes the MD volumetric flow rate.

2.3.2. Transport diffusion coefficients

The transport diffusion coefficient is a general parameter used to describe the migration capacity of isotopologues under various pressure conditions. The transport diffusivity coefficient in NEMD simulations can be calculated as (Bhatia and Nicholson, 2003; Kazemi and Takbiri-Borujeni, 2016)

$$D = \frac{k_B T \bar{j}}{\rho F} \tag{5}$$

where k_B represents the Boltzmann constant, F denotes the applied external force, T expresses the temperature and $\bar{j}$ and ρ refer to the mean mass flux and average gas density in the pores, respectively.

2.3.3. Specific enthalpy

During wall fluid scattering, the loss of energy at the interface leads to an increase in particle energy (enthalpy) of the particles (Fu et al., 2017). The specific enthalpy indicates the energy transfer of molecules within a confined area (Farago, 2019). The local specific enthalpy can be represented as (Fu et al., 2017)

$$\begin{cases} h(z) = u(z) + p(z) \\ h(z^*) = u(z^*) + p(z^*) \end{cases} \tag{6}$$

where $u(z)$ represents sum of the kinetic and potential energy, and $p(z)$ expresses the virial pressure expression. Due to the different flow behaviors exhibited by isotopic gases, the kinetic and potential energies of isotopic methane gases near the surface of the pore wall vary (Zhang et al., 2020b). As a result, the enthalpy of the isotope methane gas changes as it slides along the wall.

3. Results and discussions

3.1. Density distribution of methane isotopic gas at the equilibrium state

Methane isotope fractionation generally occurred in both thermodynamic equilibrium and kinetic mechanisms (Xia and Tang, 2012). Fig. 3 showed the density distribution of methane isotopes in 3 nm pores ($\Delta P = 20$ MPa) under the condition of water absence and water presence (with water saturation of 30.44%) at a temperature of 350 K.

In the absence of water in the pore, a density adsorption layer was formed between methane molecules and the pore surface due to Van der Waals interaction (Sui and Yao, 2016). Moreover, within the adsorption layer of nanopores, the density of $^{13}CH_4$ molecules was slightly higher than that of $^{12}CH_4$ molecules since $^{13}CH_4$ molecules with larger physical mass were more easily trapped on the pore surface (Liu et al., 2016). The gas density distributions of $^{13}CH_4$ and $^{12}CH_4$ were also examined in the simulation. Fig. 4 presented the density profiles of $^{12}CH_4$ and $^{13}CH_4$ at a temperature of 350 K and a pressure difference of 20 MPa. The adsorption layer density of $^{13}CH_4$ (424.08 kg/m^3 for water-free pore and 278.96 kg/m^3 for water-filled pore) was greater than that of $^{12}CH_4$ (356.39 kg/m^3 for water-free pore and 237.59 kg/m^3 for water-filled pore). Compared to isotopic gases, water molecules were preferentially occupied on adsorption sites of the hydrophilic inorganic pore surface, and formed a higher-density adsorption layer.

3.2. Transport properties and mechanisms of $^{12}CH_4$ and $^{13}CH_4$

3.2.1. Velocity distributions of $^{12}CH_4$ and $^{13}CH_4$

In the nanopores, movement of isotopic gas molecules in the pores was mostly driven by the pressure difference (Liu et al., 2016). The velocity distributions of $^{12}CH_4$ and $^{13}CH_4$ molecules under anhydrous and aqueous conditions at 350 K and 20 MPa were illustrated in Fig. 5. It was found that the velocity of isotopic gases exhibited a Poiseuille distribution with higher velocity in the bulk areas. However, the velocity of the $^{12}CH_4$ molecules was higher than that of the $^{13}CH_4$ molecules both under the absence and presence of water conditions. This was because $^{12}CH_4$ molecules with lighter mass had higher mobile capacity (Todd et al., 1995).

In addition, the velocity of the $^{12}CH_4$ and $^{13}CH_4$ isotopic gases showed a decreasing trend when water molecules were present in the inorganic pores. This was mainly due to the presence of water molecules that enhanced the viscous interaction between methane molecules, thereby inhibiting their flow velocity (Zheng et al., 2023). In hydrophilic nanopores, the presence of the water film in gas-liquid two-phase flow reduced the effective radius of the pores, intensifying the confinement effect on gases and consequently leading to a decline in the velocity of isotopic gases. Furthermore, the reduction in effective pore size (D_{eff}) resulted in an increase in the Knudsen number (Kn), which enhanced the non-continuum flow effects observed in isotopic gases.

3.2.2. Water distribution on the inorganic pore

The inorganic pores formed hydrogen bonds with water molecules due to their hydrophilic groups (Christoph Hartnig and Rovere, 2000). When the water saturation was 7.61% and 15.23%, the water molecules formed a thin water film inside the channel, and the isotope gas molecules had a large diffusion area (Fig. 6(a) and (b)). Due to the non-uniform distribution of hydroxyl groups on the surface of silica, under low water saturation conditions, water molecules were preferentially adsorbed to the hydrophilic region with high hydroxyl density on the surface through

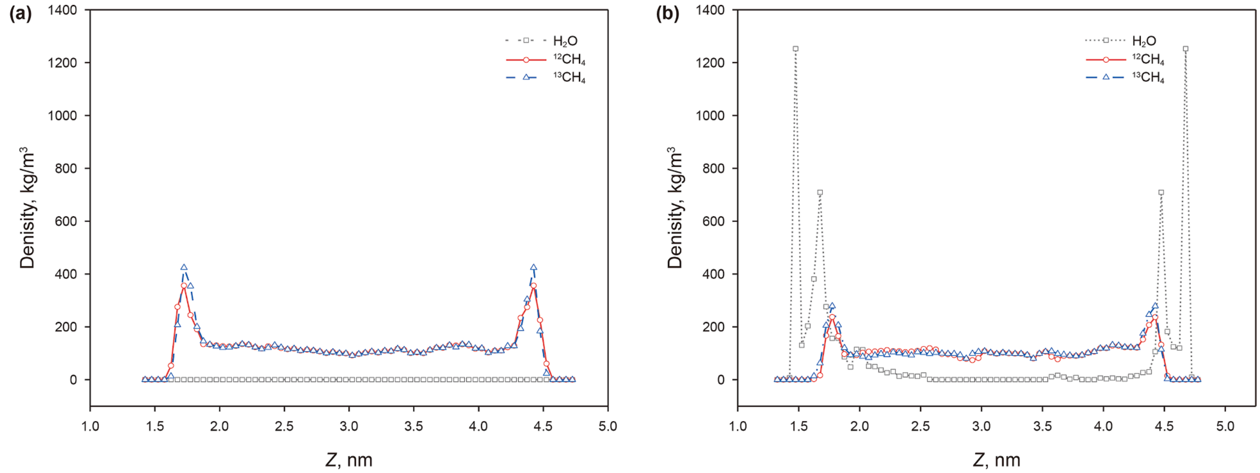

Fig. 3. Density distribution of CH_4 and H_2O molecules in inorganic pores of **(a)** no water; **(b)** water saturation (30.44%).

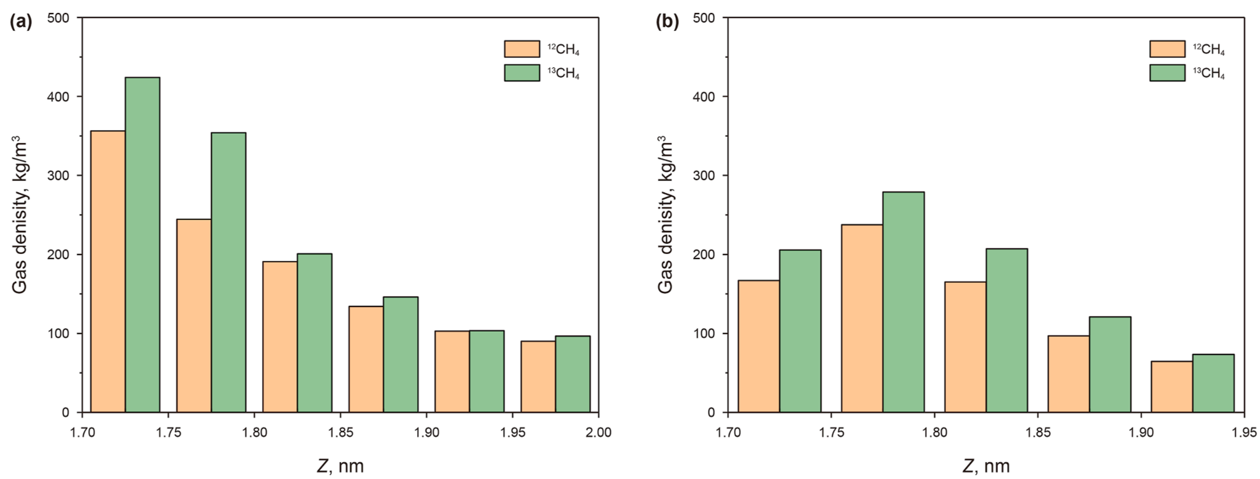

Fig. 4. Maximum gas density layer of **(a)** no water; **(b)** water saturation (30.44%).

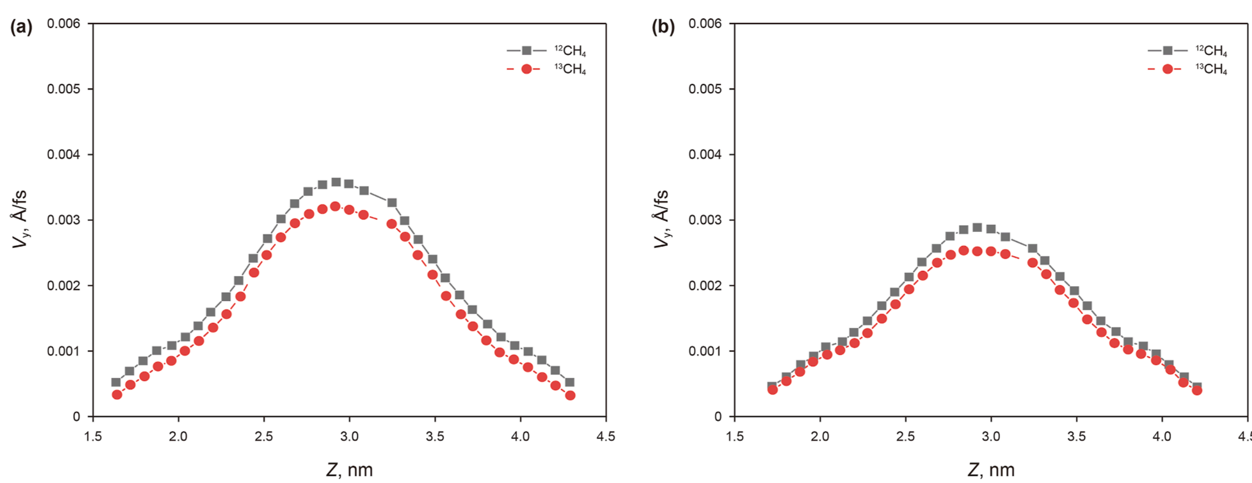

Fig. 5. Velocity profiles of $^{12}CH_4$ and $^{13}CH_4$ molecules in **(a)** no water; **(b)** water saturation (30.44%).

hydrogen bonding (Collin et al., 2018). This led to local nucleation and clustering, and finally resulted in the formation of a water film with heterogeneous characteristics. As the water saturation increased to 30.44%, the water molecules adsorbed on the wall surface began to connect with each other gradually, leading to a reduction in the effective flow area within the pore (Fig. 6(c)).

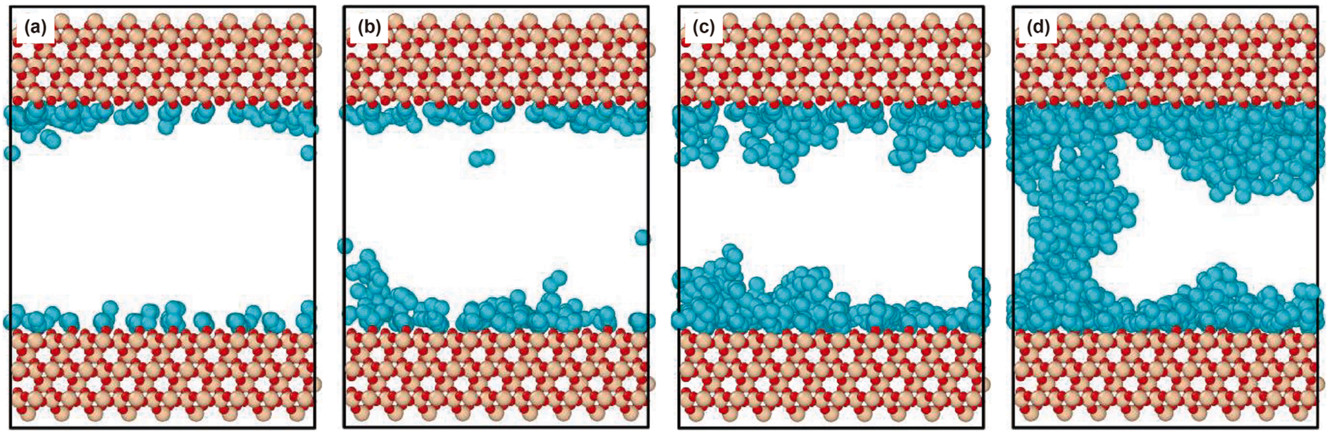

Fig. 6. The distribution of water within silica channels at different water saturation: **(a)** 7.61%; **(b)** 15.23%; **(c)** 30.44%; **(d)** 44.66%.

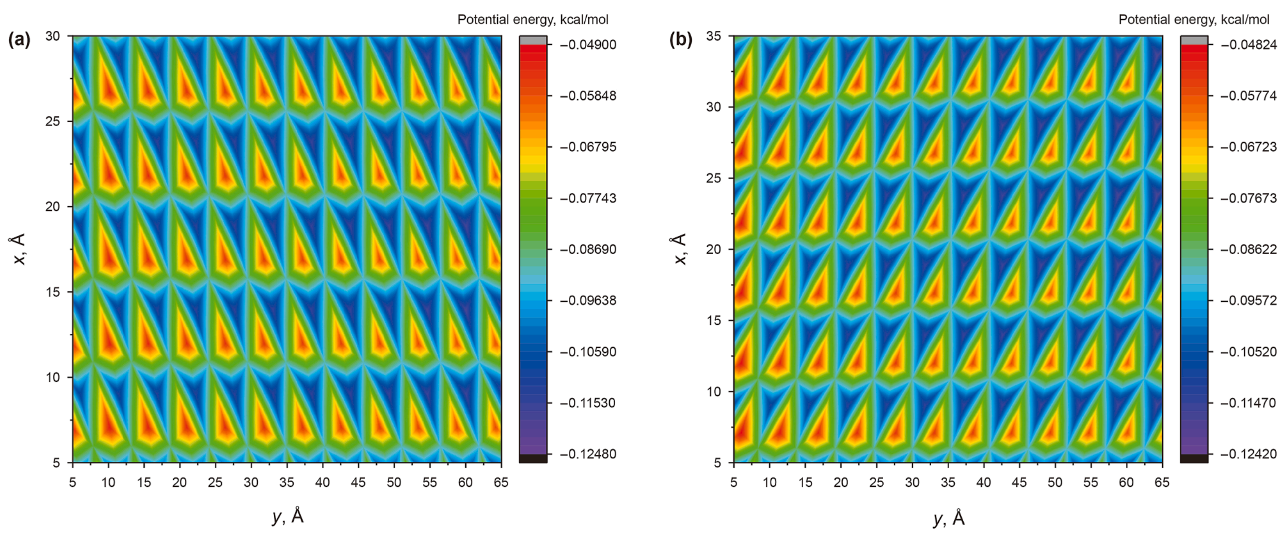

Fig. 7. Potential energy surface (PES) maps of **(a)** anhydrous pore surface; **(b)** hydrous pore surface.

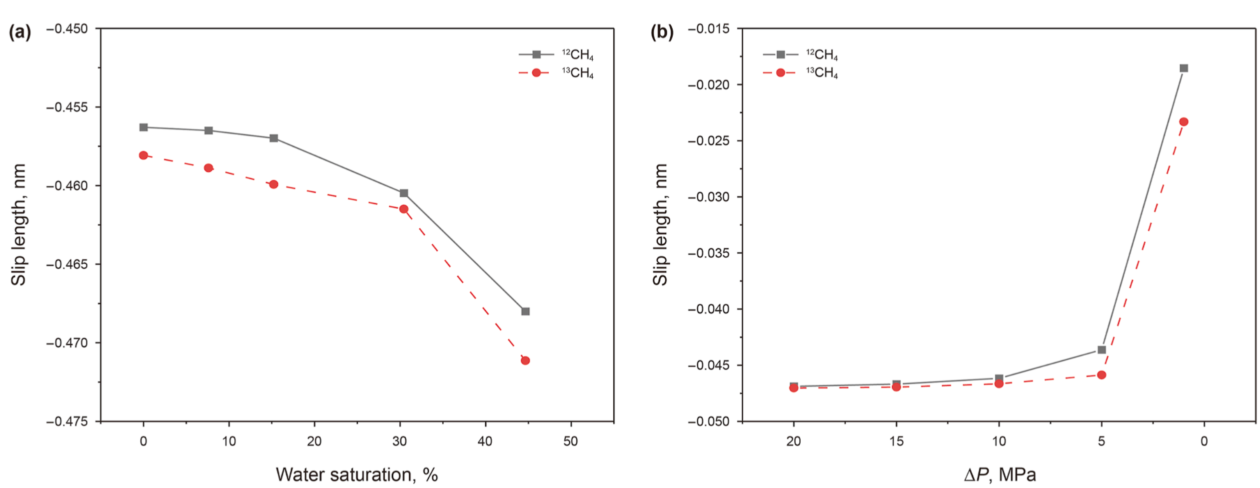

Fig. 8. Slip length **(a)** at different water saturation and **(b)** at different pressure gradients.

Water bridges formed when the water saturation exceeded 30.44%, the presence of water bridges hindered the movement of isotopic gases within the channel (Fig. 6(d)).

3.2.3. Potential energy distributions

The roughness of the pore wall was changed by the presence of water in the channel. The nanoscale surface roughness was characterized by the potential energy surface (PES) (Yu et al., 2020a). Therefore, the roughness could be determined by calculating the standard deviation of the PES (Yu et al., 2020b; Wang et al., 2021a), which was a critical factor affecting isotope fractionation. The potential energy profiles under anhydrous and hydrous conditions were illustrated in Fig. 7(a) and (b), respectively. The potential energy range of the anhydrous wall surface (minimum: −0.1248 kcal/mol; maximum: −0.049 kcal/mol) was lower than that of hydrous wall surface (minimum: −0.1242 kcal/mol; maximum: −0.048 kcal/mol). This indicated that the hydrophilic pores had a stronger adsorption capacity for methane in the absence of water due to the deeper potential well depth exerted by the pore walls on gas molecules.

The PES roughness for the anhydrous pore (0.02499 kcal/mol) was higher than that for the hydrous pore (0.002457 kcal/mol), suggesting that the hydrous pore surface was smoother than the anhydrous pore surface. The smoother surface pores exhibited enhanced specular reflection of methane isotopologues, which promoted rapid surface diffusion and frictionless gas flow (Yu et al., 2020b). As a result, methane isotope fractionation was intensified when water molecules were present in silica channels.

3.2.4. Slip length

Based on the magnitude of the Knudsen number, the main form of flow transport of isotopes in the pores was located in the transition flow (Zhang et al., 2019), where a certain degree of slip effect was present in the motion of isotopic gases. Fig. 8 showed the slip lengths of $^{12}CH_4$ and $^{13}CH_4$, it was found that the slip length of $^{12}CH_4$ exceeded that of $^{13}CH_4$. As compared to $^{12}CH_4$ molecules, $^{13}CH_4$ molecules had more friction and less slip due to their greater physical mass, resulting in reduced slip lengths. The variation in slip lengths of isotopic gases under varying water saturation conditions at a constant pressure (20 MPa) was given in Fig. 8(a). The slip lengths of both $^{12}CH_4$ and $^{13}CH_4$ molecules exhibited a monotonic decreasing trend as the water molecule saturation increased. Inorganic pores with rough surfaces underwent negligible slippage due to the large consumption of tangential momentum of methane isotopes (Yu et al., 2020b). Additionally, the formation of the water film reduced the effective flow area for isotope molecules, thereby increasing the collision frequency between isotope gas molecules, which was manifested as enhanced viscous flow. During the collision process, the continuous increase in energy dissipation of methane molecules led to a decrease in their flow velocity and simultaneously weakened the slip effect.

In addition, the variation in slip lengths of isotopic gases under varying driving forces with the same water saturation (30.44%) was also given in Fig. 8(b). With the increase of pressure difference, the slip lengths of $^{12}CH_4$ and $^{13}CH_4$ molecules both showed a monotonously decreasing trend. With the increase in pressure difference, the effective mean free path of the isotope gas diminished (Cao et al., 2009). The increase in viscosity led to additional viscous dissipation, which reduced boundary slip, resulting in a decreasing trend in the slip length (Bao et al., 2017). As a result, the difference in slip behavior between $^{12}CH_4$ and $^{13}CH_4$ molecules on the surface of inorganic pores in the absence and presence of water had a relatively small impact on the fractionation of methane isotopes.

3.2.5. Enthalpy profiles

The specific enthalpy reflected the energy variation in the process of wall-fluid scattering, which resulted in the difference in the mobility of isotopic gases (Farago, 2019). The specific enthalpy curves of $^{12}CH_4$ and $^{13}CH_4$ molecules with and without water were given in Fig. 9(a) and (b). It was found that the specific enthalpy of methane molecules varied in a small range in the bulk of the pore

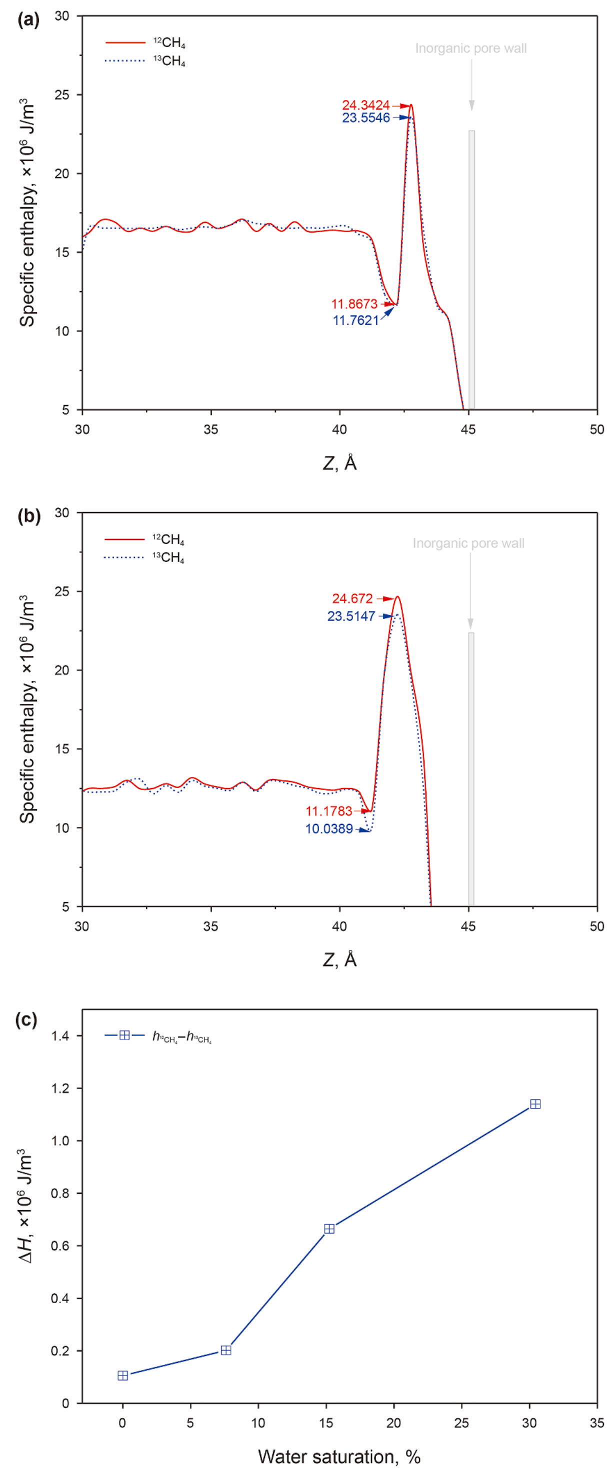

Fig. 9. Special enthalpy at pressure difference (20 MPa): **(a)** no water; **(b)** water saturation (30.44%); **(c)** the enthalpy difference of isotope gases under different water saturation conditions.

while it oscillated significantly near the surface of the pore. As the molecules approached the wall of the pore, the specific enthalpy initially dropped as the molecules neared the bottom of the potential well, and then increased as the molecules were repelled by the pore wall and acquired energy. The results were similar to Zhang et al. (2020b).

Additionally, the specific enthalpy of the $^{12}CH_4$ molecules was higher at both the negative peak point and positive peak point than that of the $^{13}CH_4$ molecules, indicating that the $^{12}CH_4$ molecules had more potential and kinetic energy than the $^{13}CH_4$ molecules. Therefore, there were differences in the specific enthalpy changes (ΔH) of $^{12}CH_4$ and $^{13}CH_4$ molecules as they approached the bottom of the potential well under both anhydrous and hydrated conditions. Specifically, the specific enthalpy differences ($\Delta h_{^{12}C\_nega}$ and $\Delta h_{^{13}C\_nega}$) between anhydrous and hydrated conditions were 0.69 J/m^3 (11.87 − 11.18 = 0.69) and 1.72 J/m^3 (11.76 − 10.04 = 1.72) at negative peak points, respectively. Therefore, higher energy loss occurred for $^{13}CH_4$ molecules diffusion in nano-sized pores when transitioning from single-phase flow to two-phase flow (water-gas) conditions. As the water saturation increased from 0% to 30.44%, the enthalpy difference ($\Delta h_{^{12}C\_^{13}C}$) between $^{12}CH_4$ molecules and $^{13}CH_4$ molecules gradually increased, indicating that the water molecules increased the energy barrier that the isotope gas needed to overcome during diffusion (Fig. 9(c)). With more water inside the inorganic (hydrophilic) pore, water films were attached to the pore surface, leading to a decrease in the effective pore size and a reduction in the motion area. These changes resulted in a deeper attractive potential which hindered the molecules diffusion in the bulk areas. Furthermore, the presence of water molecules enhanced the viscous flow of isotope gases. Thus, $^{13}CH_4$ molecules with larger physical mass experienced more energy loss during the two-phase flow process. As a result, the enhanced enthalpy difference ($\Delta h_{^{12}C\_^{13}C}$) during two-phase flow led to a more pronounced isotope fractionation.

3.2.6. Transport diffusivity

In two-phase flow (water saturation: 30.44%), the transport diffusion coefficients of both $^{12}CH_4$ (D) and $^{13}CH_4$ (D^*) decreased as the differential pressure decreased (Fig. 10(a)). The transport diffusivity of $^{12}CH_4$ (D) and $^{13}CH_4$ (D^*) was of the order of −9, which was close to other researches (Charrière et al., 2010; Zhang et al., 2020b). During diffusion, the increase in the driving force (differential pressure) accelerated the transport of gas molecules.

Furthermore, the diffusion coefficient of isotopic gases decreased as the water saturation increased (Fig. 10(b)) at a constant pressure difference of 20 MPa. An increase in water saturation resulted in a decrease in pore size, leading to a more pronounced confinement effect of the wall surface on gas molecules. Gas-wall interactions were more prominent in the smaller pores (Li et al., 2019), leading to a smaller transport diffusion coefficient. The greater physical mass and enhanced interaction energy between the gas and the walls led to a more pronounced reduction in the diffusion coefficient of $^{13}CH_4$ molecules, as these molecules lost more energy during the process. Under all conditions of pressure differential and water saturation, D was consistently greater than D^*. Due to the different physical qualities of $^{12}CH_4$ and $^{13}CH_4$, the $^{12}CH_4$ molecules have moved faster than $^{13}CH_4$ (Chen et al., 2016).

3.3. Methane carbon isotope fractionation in two-phase flow

The ratio of the diffusion coefficient (D^*) of $^{13}CH_4$ to diffusion coefficient (D) of $^{12}CH_4$ is denoted as (D^*/D). This ratio is established to assess the extent of carbon isotope fractionation (Wang et al., 2021a). Thus, the lower the D^*/D ratio, the greater the degree of isotope fractionation. According to Fig. 11(a), the D^*/D values exhibited two stages fractionation with the decrease of pressure at water saturation of 30.44%. In the initial phase (the pressure difference decreasing from 20 to 7 MPa), the value of D^*/D decreased, and then, the D^*/D value increased as the pressure was below the critical pressure. As previously mentioned, the lighter $^{12}CH_4$ molecules were preferentially desorbed with the decline in pressure difference, and the degree of methane isotope fractionation increased. When the pressure dropped to a critical pressure, the heavy $^{13}CH_4$ molecules began to desorb, resulting in a reduced degree of isotope fractionation (Li et al., 2022).

Similarly, the D^*/D values did not exhibit a monotonically increasing trend with the increase in water saturation (Fig. 11(b)). After the system reached equilibrium, the isotopic fractionation primarily arose from differential diffusion kinetics between the isotopic molecules ($^{12}CH_4$ and $^{13}CH_4$) rather than adsorption/desorption dynamics, since the system pressure almost remained constant. As the water saturation increased from 0% to 30.44%, the D^*/D values demonstrated a decreasing trend, in other words, fractionation intensified. In this stage, water molecules formed water films in the inorganic pores, reducing effective pore size. As discussed above, the reduction in effective pore diameter led to an increase in the Knudsen number, thereby enhancing the

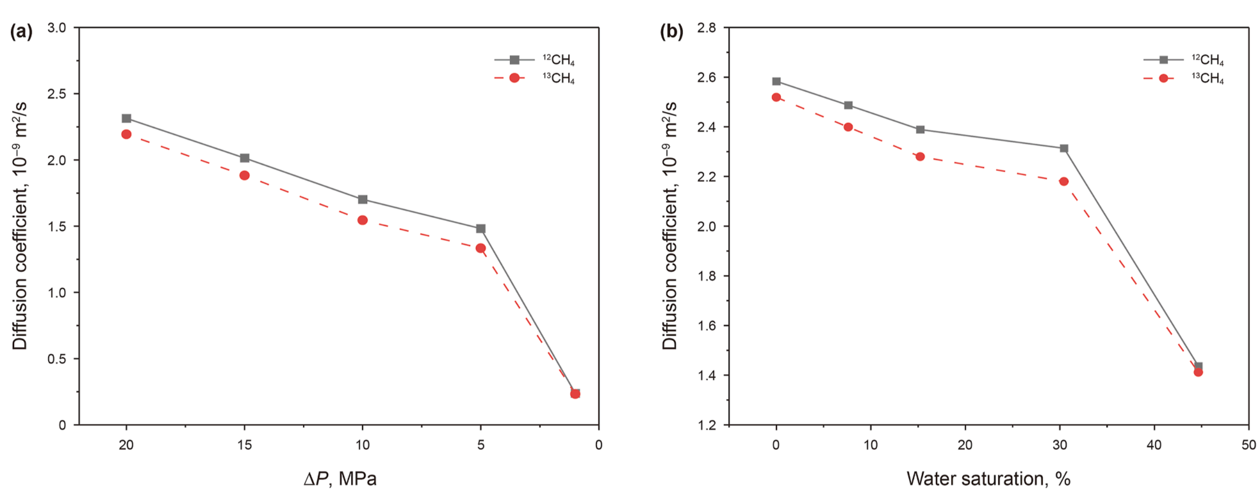

Fig. 10. Diffusion coefficient **(a)** at different pressure gradients and **(b)** at different water saturation.

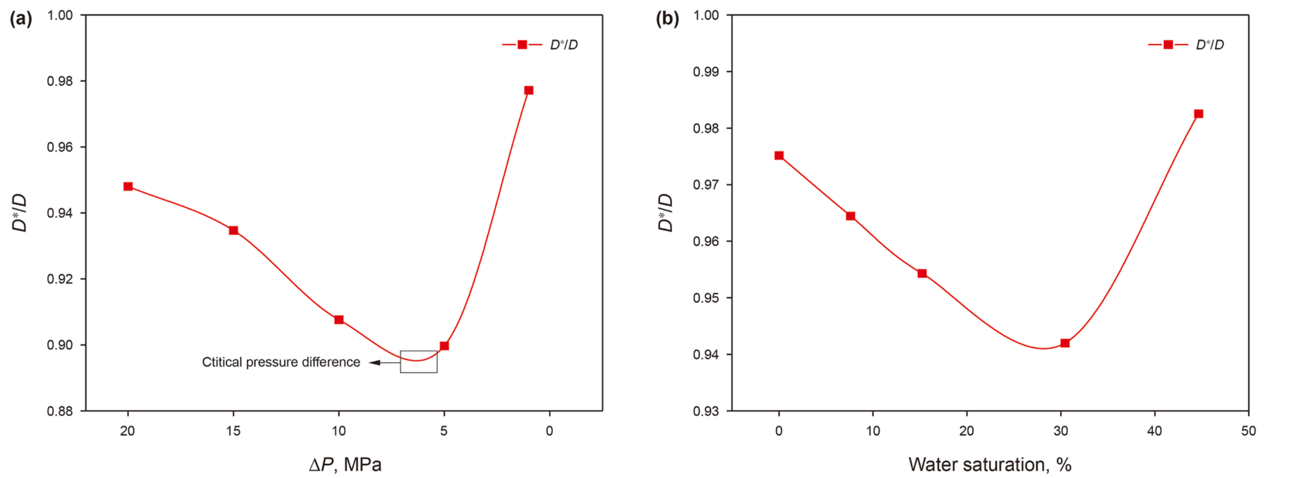

Fig. 11. The extent of carbon isotope fractionation under **(a)** at different pressure gradients at a constant water saturation (30.44%) and **(b)** at different water saturation at a constant pressure (20 MPa).

discontinuous flow effects of isotopic gases. This finding was consistent with the conclusion of Wang et al., which stated that the smaller the size of the inorganic pore, the more significant the gas isotope fractionation effect (Wang et al., 2021a). The intensified non-continuous flow between the fluid and the pore surface accelerated the fractionation process (Bao et al., 2017; Li et al., 2019). Therefore, as the number of water molecules increased, the diffusion rate of $^{13}CH_4$ molecules decreased more than that of $^{12}CH_4$ molecules, resulting in an enhancement of the degree of isotope fractionation.

When the saturation of water molecules increased further (>30.44%), water bridge structures formed within the inorganic pores (Fig. 6). The presence of these water bridges significantly hindered the movement and diffusion of isotopic gases. In this case, the degree of isotope fractionation was weakened due to the restricted migration of isotopic gases within the pores.

4. Conclusions

In this study, molecular dynamics (MD) simulations were employed to explore the isotopic species ($^{12}CH_4$ and $^{13}CH_4$) fractionation within silica channels under varying water saturation at a constant pressure gradient of 20 MPa. The principal findings derived from the conducted simulation are delineated as follows:

(1) In hydrophilic nanopores, water molecules predominantly occupied the adsorption sites, creating a layer of water film (the water saturation <30.44%), which resulted in a decrease in the isotopic gas adsorption layer density and enhanced the confinement effect of the pore walls on the isotopic gases, leading to a reduction in the velocities of both $^{12}CH_4$ and $^{13}CH_4$ molecules.

(2) When the water saturation in the pores increased from 0% to 30.44%, the degree of fractionation of methane isotopes increased. The diffusion coefficient of $^{13}CH_4$ decreased more significantly than that of $^{12}CH_4$ due to the larger molecular mass, resulting in a decreasing trend in D^*/D. Meanwhile, the enthalpy difference ($\Delta h_{^{12}C-^{13}C}$) between $^{12}CH_4$ molecules and $^{13}CH_4$ molecules increased. Water bridges began to form in the inorganic pores when the water saturation was greater than 30.44%, which hindered the flow of isotope gases, and D^*/D began to increase.

(3) The enhancement of isotope fractionation effect by water confined in hydrophilic nanopores can be attributed to two synergistic mechanisms: Firstly, the coupling effect of the gas-liquid-solid interface of the water film in hydrophilic pores significantly enhanced Knudsen diffusion by reducing the effective pore size. Secondly, the presence of the water film made the pore wall smoother, thereby increasing the difference in the movement of isotope molecules.

(4) In the simulation, the presence of the water film changed the relative velocity of the three phases (among methane isotopic gases, water, and pore surface) when the driving force in the inorganic pore was changed (from 20 MPa to 1 MPa), and the degree of isotope fractionation showed a trend of first increasing and then weakening.

This study advanced the understanding of carbon isotope fractionation by integrating aqueous phase effects beyond single-phase models, better reflecting reservoir conditions. A correlation between isotopic fractionation and water saturation was established, enabling diagnostic tools to monitor water encroachment and optimize production strategies.

CRediT authorship contribution statement

Pei-Qi Xu: Methodology, Data curation, Writing – original draft, Formal analysis. **Wei Chen:** Conceptualization, Writing – review & editing.

Declaration of competing interest

The authors declare that they have no known competing financial interests or personal relationships that could have appeared to influence the work reported in this paper.

Acknowledgement

The authors wish to acknowledge the financial support from the National Natural Science Foundation of China, China (Grant 51776132) and the Key Laboratory of Coalbed Methane Resources and Reservoir Formation Process of the Ministry of Education (China University of Mining and Technology) (No. 2024-007).

References

Aranovich, G.L., Donohue, M.D., 2009. Diffusion in fluids with large mean free paths: non-classical behavior between Knudsen and Fickian limits. Phys. Stat. Mech. Appl. 388, 3355–3370. https://doi.org/10.1016/j.physa.2009.05.012.

Arif, M., Zhang, Y., Iglauer, S., 2021. Shale wettability: data sets, challenges, and outlook. Energy Fuel 35, 2965–2980. https://doi.org/10.1021/acs.energyfuels.0c04120.

Babaei, S., Ghasemzadeh, H., Tesson, S., 2023. Methane adsorption of nanocomposite shale in the presence of water: insights from molecular simulations. Chem. Eng. J. 475, 146196. https://doi.org/10.1016/j.cej.2023.146196.

Bao, L., Priezjev, N.V., Hu, H., Luo, K., 2017. Effects of viscous heating and wall-fluid interaction energy on rate-dependent slip behavior of simple fluids. Phys. Rev. E. 96, 033110. https://doi.org/10.1103/PhysRevE.96.033110.

Bhatia, S.K., Nicholson, D., 2003. Hydrodynamic origin of diffusion in nanopores. Phys. Rev. Lett. 90, 16105. https://doi.org/10.1103/PhysRevLett.90.016105.

Bui, T., Phan, A., Cole, R.D., Striolo, A., 2017. Transport mechanism of guest methane in water-filled nanopores. J. Phys. Chem. C 121, 15675–15686. https://doi.org/10.1021/acs.jpcc.7b02713.

Cao, B.Y., Sun, J., Chen, M., Guo, Z.Y., 2009. Molecular momentum transport at fluid-solid interfaces in MEMS/NEMS: a review. Int. J. Mol. Sci. 10, 4638–4706. https://doi.org/10.3390/ijms10114638.

Charrière, D., Pokryszka, Z., Behra, P., 2010. Effect of pressure and temperature on diffusion of CO_2 and CH_4 into coal from the Lorraine basin (France). Int. J. Coal Geol. 81, 373–380. https://doi.org/10.1016/j.coal.2009.03.007.

Chen, C.Y., Horne, R.N., 2006. Two-phase flow in rough-walled fractures: experiments and a flow structure model. Water Resour. Res. 42, W03430. https://doi.org/10.1029/2004wr003837.

Chen, F., Jiang, C., Shi, P., et al., 2016. Geochemical characteristics of terrestrial shale gas and its production prediction significance in the Ordos Basin, China. J Nat. Gas Geosci. 1, 425–433. https://doi.org/10.1016/j.jnggs.2016.11.007.

Chen, G., Lu, S., Liu, K., et al., 2020. Occurrence state and micro mechanisms of shale gas on pore walls. Earth Sci. J. China Univ. Geosci. 45, 1782–1790. https://doi.org/10.3799/dqkx.2019.194.

Chen, J., Yu, H., Fan, J., et al., 2017. Channel-width dependent pressure-driven flow characteristics of shale gas in nanopores. AIP Adv. 7, 045217. https://doi.org/10.1063/1.4982729.

Chen, Y., Jing, J., Karimov, R., et al., 2024. Experimental investigation on flow patterns and pressure gradients of shale oil–water flow in a horizontal pipe. Int. J. Multiphas. Flow 176, 104839. https://doi.org/10.1016/j.ijmultiphaseflow.2024.104839.

Chen, Z., Feng, D., Wu, K., et al., 2023. Quantificational determination of methane adsorption in organic matter and inorganic matter of shale rocks. J. Univ. Pet., China (Ed. Nat. Sci.) 47, 65–75 (in Chinese).

Christoph Hartnig, W.W., Rovere, A.R.M., 2000. Modifications of the hydrogen bond network of liquid water in a cylindrical SiO_2 pore. J. Mol. Liq. 85, 127–137.

Collin, M., Gin, S., Dazas, B., et al., 2018. Molecular dynamics simulations of water structure and diffusion in a 1 nm diameter silica nanopore as a function of surface charge and alkali metal counterion identity. J. Phys. Chem. C 122, 17764–17776. https://doi.org/10.1021/acs.jpcc.8b03902.

Darden, T., York, D., Pedersen, L., 1993. Particle mesh Ewald: an N·log(N) method for Ewald sums in large systems. J. Chem. Phys. 98, 10089–10092. https://doi.org/10.1063/1.464397.

Farago, O., 2019. A simple statistical-mechanical interpretation of Onsager reciprocal relations and Derjaguin theory of thermo-osmosis. Eur. Phys. J. E Soft Matter 42, 136. https://doi.org/10.1140/epje/i2019-11898-3.

Feng, Y., Xiao, X.M., Wang, E.Z., et al., 2023. Gas storage in shale pore system: a review of the mechanism, control and assessment. Pet. Sci. 20, 2605–2636. https://doi.org/10.1016/j.petsci.2023.05.012.

Fu, L., Merabia, S., Joly, L., 2017. What controls thermo-osmosis? Molecular simulations show the critical role of interfacial hydrodynamics. Phys. Rev. Lett. 119, 214501. https://doi.org/10.1103/PhysRevLett.119.214501.

Gong, L., Shi, J.H., Ding, B., et al., 2020. Molecular insight on competitive adsorption and diffusion characteristics of shale gas in water-bearing channels. Fuel 278, 118406. https://doi.org/10.1016/j.fuel.2020.118406.

Hantal, G., Brochard, L., Dias Soeiro Cordeiro, M.N., et al., 2014. Surface chemistry and atomic-scale reconstruction of kerogen–silica composites. J. Phys. Chem. C. 118, 2429–2438. https://doi.org/10.1021/jp406329n.

He, M., Sun, X., Zhao, J., 2014. Advances in interaction mechanism of water (gas) on clay minerals in China. Int. J. Min. Sci. Technol. 24, 727–735. https://doi.org/10.1016/j.ijmst.2014.10.009.

Kazemi, M., Takbiri-Borujeni, A., 2016. Non-equilibrium molecular dynamics simulation of gas flow in organic nanochannels. J. Nat. Gas Sci. Eng. 33, 1087–1094. https://doi.org/10.1016/j.jngse.2016.05.068.

Li, W., Lu, S., Li, J., et al., 2022. Research progress on isotopic fractionation in the process of shale gas/coalbed methane migration. Petrol. Explor. Dev. 49, 1069–1084. https://doi.org/10.1016/s1876-3804(22)60333-1.

Li, Y., Hu, Z., Duan, X., et al., 2019. The general form of transport diffusivity of shale gas in organic-rich nano-slits—A molecular simulation study using Darken approximation. Fuel 249, 457–471. https://doi.org/10.1016/j.fuel.2019.03.074.

Liu, B., Qi, C., Zhao, X., et al., 2018. Nanoscale two-phase flow of methane and water in shale inorganic matrix. J. Phys. Chem. C. 122, 26671–26679. https://doi.org/10.1021/acs.jpcc.8b06780.

Liu, P., Wang, X., Lin, Y., et al., 2020. Chemical and carbon isotope fractionations of alkane gases desorbed from confined systems and the application toward shale gas reservoir. Mar. Petrol. Geol. 113, 104103. https://doi.org/10.1016/j.marpetgeo.2019.104103.

Liu, Y., Liang, F., Shang, F., et al., 2023. Carbon isotope fractionation during shale gas release: Experimental results and molecular modeling of mechanisms. Gas Sci. Eng. 113, 204962. https://doi.org/10.1016/j.jgsce.2023.204962.

Liu, Y., Zhang, Jinchuan, Tang, X., 2016. Predicting the proportion of free and adsorbed gas by isotopic geochemical data: A case study from lower permian shale in the southern north china basin (SNCB). Int. J. Coal Geol. 156, 25–35. https://doi.org/10.1016/j.coal.2016.01.011.

Martin, M.G., Siepmann, J.I., 1998. Transferable potentials for phase equilibria. 1. United-Atom Description of n-Alkanes. J. Phys. Chem. B 102, 2569–2577.

Merzel, F., Avbelj, F., 2020. Why do water molecules around small hydrophobic solutes form stronger hydrogen bonds than in the bulk? Biochim. Biophys. Acta Gen. Subj. 1864, 129537. https://doi.org/10.1016/j.bbagen.2020.129537.

Mo, F., Qi, Z., Huang, X., et al., 2022. Knudsen diffusion in pore-scale water-bearing shales: Modelling and case study. J. Petrol. Sci. Eng. 214, 110457. https://doi.org/10.1016/j.petrol.2022.110457.

Mo, F., Qi, Z., Yan, W., et al., 2020. Influence of water on gas transport in shale nanopores: Pore-scale simulation study. Energy Fuel 34, 8239–8249. https://doi.org/10.1021/acs.energyfuels.0c01278.

Nan, Y., Li, W., Jin, Z., 2020. Slip length of methane flow under shale reservoir conditions: effect of pore size and pressure. Fuel 259, 116237. https://doi.org/10.1016/j.fuel.2019.116237.

Qin, Z., Suckale, J., 2017. Direct numerical simulations of gas–solid–liquid interactions in dilute fluids. Int. J. Multiphas. Flow 96, 34–47. https://doi.org/10.1016/j.ijmultiphaseflow.2017.07.008.

Qu, Z., Sun, J., Shi, J., et al., 2016. Characteristics of stable carbon isotopic composition of shale gas. J Nat. Gas Geosci. 1, 147–155. https://doi.org/10.1016/j.jnggs.2016.05.008.

Randall, T., Andrey, G., 2004. Molecular models of hydroxide, oxyhydroxide, and clay phases and the development of a general force field. J. Phys. Chem. 108, 1255–1266.

Richter, F.M., Mendybaev, R.A., Christensen, J.N., et al., 2006. Kinetic isotopic fractionation during diffusion of ionic species in water. Geochem. Cosmochim. Acta 70, 277–289. https://doi.org/10.1016/j.gca.2005.09.016.

Sui, H., Yao, J., 2016. Effect of surface chemistry for CH_4/CO_2 adsorption in kerogen: a molecular simulation study. J. Nat. Gas Sci. Eng. 31, 738–746. https://doi.org/10.1016/j.jngse.2016.03.097.

Sun, C., Nie, H., Dang, W., et al., 2021. Shale gas exploration and development in China: Current status, geological challenges, and future directions. Energy Fuel 35, 6359–6379. https://doi.org/10.1021/acs.energyfuels.0c04131.

Sun, Z., Shi, J., Wang, K., et al., 2018. The gas-water two phase flow behavior in low-permeability CBM reservoirs with multiple mechanisms coupling. J. Nat. Gas Sci. Eng. 52, 82–93. https://doi.org/10.1016/j.jngse.2018.01.027.

Thomas, J.A., McGaughey, A.J., 2009. Water flow in carbon nanotubes: transition to subcontinuum transport. Phys. Rev. Lett. 102, 184502. https://doi.org/10.1103/PhysRevLett.102.184502.

Todd, B.D., Evans, D.J., Daivis, P.J., 1995. Pressure tensor for inhomogeneous fluids. Phys. Rev. E 52, 1627–1638. https://doi.org/10.1103/physreve.52.1627.

Veltzke, T., Thöming, J., 2012. An analytically predictive model for moderately rarefied gas flow. J. Fluid Mech. 698, 406–422. https://doi.org/10.1017/jfm.2012.98.

Wan, X., Liu, C., Zhao, D., Ge, X., 2023. Hotspot and development trend of shale oil research. Earth Sci. 48 (2), 793–802. https://doi.org/10.3799/dqkx.2022.443.

Wang, G., Ma, Y., Chen, W., 2022. Molecular level study of carbon isotope fractionation in Knudsen number flows induced by thermo-osmosis. Int. J. Therm. Sci. 174, 107441. https://doi.org/10.1016/j.ijthermalsci.2021.107441.

Wang, G., Ma, Y., Zhao, Y., Chen, W., 2021a. Carbon isotope fractionation during shale gas transport through organic and inorganic nanopores from molecular simulations. Energy Fuel. 35, 11992–12004. https://doi.org/10.1021/acs.energyfuels.1c01448.

Wang, S., Feng, Q., Javadpour, F., et al., 2019. Competitive adsorption of methane and ethane in montmorillonite nanopores of shale at supercritical conditions: a grand canonical Monte Carlo simulation study. Chem. Eng. J. 355, 76–90. https://doi.org/10.1016/j.cej.2018.08.067.

Wang, S., Feng, Q., Zha, M., et al., 2017a. Supercritical methane diffusion in shale nanopores: effects of pressure, mineral types, and moisture content. Energy Fuel. 32, 169–180. https://doi.org/10.1021/acs.energyfuels.7b02892.

Wang, S., Shi, J., Wang, K., et al., 2017b. New coupled apparent permeability models for gas transport in inorganic nanopores of shale reservoirs considering multiple effects. Energy Fuel 31, 13545–13557. https://doi.org/10.1021/acs.energyfuels.7b02948.

Wang, S., Yao, X., Feng, Q., et al., 2021b. Molecular insights into carbon dioxide enhanced multi-component shale gas recovery and its sequestration in realistic kerogen. Chem. Eng. J. 425, 130292. https://doi.org/10.1016/j.cej.2021.130292.

Wei, Y., Lu, S., Li, J., et al., 2021. Impacts of gas pressure on carbon isotope fractionation during methane degassing—An experimental study on shales from Wufeng and Longmaxi Formations in southeast Sichuan, China. Mar. Petrol. Geol. 128, 105001. https://doi.org/10.1016/j.marpetgeo.2021.105001.

Wu, K., Chen, Z., Li, X., 2015. Real gas transport through nanopores of varying cross-section type and shape in shale gas reservoirs. Chem. Eng. J. 281, 813–825. https://doi.org/10.1016/j.cej.2015.07.012.

Xia, X., Tang, Y., 2012. Isotope fractionation of methane during natural gas flow with coupled diffusion and adsorption/desorption. Geochem. Cosmochim. Acta 77, 489–503. https://doi.org/10.1016/j.gca.2011.10.014.

Xiang, J., Zeng, F., Liang, H., et al., 2014. Molecular simulation of the $CH_4/CO_2/H_2O$ adsorption onto the molecular structure of coal. Sci. China Earth Sci. 57, 1749–1759. https://doi.org/10.1007/s11430-014-4849-9.

Xiao, Z., Wang, G., Wang, C., et al., 2023. Permeability evolution and gas flow in wet coal under non-equilibrium state: Considering both water swelling and process-based gas swelling. Int. J. Min. Sci. Technol. 33, 585–599. https://doi.org/10.1016/j.ijmst.2022.11.012.

Xu, Q., Zhang, R., Sheng, M., et al., 2020. Nanoscale mechanical property of marine and continental organic kerogen in shale. Chin. Chem. Lett. 31, 509–512. https://doi.org/10.1016/j.cclet.2019.04.060.

Yang, Y., Song, H., Imani, G., et al., 2024. Adsorption behavior of shale oil and water in the kerogen-kaolinite pore by molecular simulations. J. Mol. Liq. 393, 123549. https://doi.org/10.1016/j.molliq.2023.123549.

Yu, H., Fan, J., Xia, J., et al., 2020a. Multiscale gas transport behavior in heterogeneous shale matrix consisting of organic and inorganic nanopores. J. Nat. Gas Sci. Eng. 75, 103139. https://doi.org/10.1016/j.jngse.2019.103139.

Yu, H., Xu, H., Fan, J., et al., 2020b. Roughness factor-dependent transport characteristic of shale gas through amorphous kerogen nanopores. J. Phys. Chem. C 124, 12752–12765. https://doi.org/10.1021/acs.jpcc.0c02456.

Yu, H., Xu, H., Fan, J., et al., 2020c. Transport of shale gas in microporous/nanoporous media: molecular to pore-scale simulations. Energy Fuel 35, 911–943. https://doi.org/10.1021/acs.energyfuels.0c03276.

Zhan, S., Su, Y., Jin, Z., et al., 2020. Effect of water film on oil flow in quartz nanopores from molecular perspectives. Fuel 262, 116560. https://doi.org/10.1016/j.fuel.2019.116560.

Zhang, L., Shan, B., Zhao, Y., Guo, Z., 2019. Review of micro seepage mechanisms in shale gas reservoirs. Int. J. Heat Mass Tran. 139, 144–179. https://doi.org/10.1016/j.ijheatmasstransfer.2019.04.141.

Zhang, W., Feng, Q., Jin, Z., et al., 2021. Molecular simulation study of oil-water two-phase fluid transport in shale inorganic nanopores. Chem. Eng. Sci. 245, 116948. https://doi.org/10.1016/j.ces.2021.116948.

Zhang, W., Huang, Z., Li, X., et al., 2020a. Estimation of organic and inorganic porosity in shale by NMR method, insights from marine shales with different maturities. J. Nat. Gas Sci. Eng. 78, 103290. https://doi.org/10.1016/j.jngse.2020.103290.

Zhang, W., Shen, B., Chen, Y., et al., 2020b. Molecular dynamics simulations about isotope fractionation of methane in shale nanopores. Fuel 278, 118378. https://doi.org/10.1016/j.fuel.2020.118378.

Zhang, Y., He, K., Wang, X., et al., 2025. Adsorption and diffusion of shale gas in kerogen matrix: insights from molecular simulations. Fuel 386, 134246. https://doi.org/10.1016/j.fuel.2024.134246.

Zheng, C., Guo, G.J., Qin, X., et al., 2023. Molecular simulation studies on the water/methane two-phase flow in a cylindrical silica nanopore: formation mechanisms of water lock and implications for gas hydrate exploitation. Fuel 333, 126258. https://doi.org/10.1016/j.fuel.2022.126258.